An Efficient Two-scale Model for the Computation of Thermal Emission and Atmospheric Reflection From the Sea Surface

Joel T. Johnson, *Senior Member, IEEE*

***Abstract*— An efficient implementation of the two-scale model of sea surface thermal emission and atmospheric reflection is described. The model is applied in a study of the reflection of downwelling atmospheric radiation; results show that reflected downwelling radiation can increase azimuthal variations of total observed brightnesses.**

***Index Terms*— Microwave Radiometry, Sea Remote Sensing, Rough Surface Scattering**

I. Introduction

DATA from the WindSAT mission [1] is providing the first large archive of polarimetric sea brightness data. Physical models of this dataset are of interest in wind vector retrieval applications, as well as for improving understanding of the emission physics involved. The two-scale model is an approximate theory of sea emission that has been applied in several studies ([2]-[11]) to analyze measured data, primarily from ground-based or aircraft missions prior to the WindSAT launch. Although other approximate theories are available for comparing with data [12]-[16], previous studies have yet to demonstrate any conclusive advantages over or general inaccuracies in the two-scale theory. Numerical methods for computing rough surface thermal emission [17]-[18] remain too computationally expensive to be practical for general use at present. For this reason, use of the two-scale model for comparison with the WindSAT dataset remains highly relevant.

As described in [3], the two-scale model is based on a separation of the sea-surface into "long" and "short" wave regions, with the choice of the separation point a free parameter. Sea-surface waves in the "long" region contribute to the long wave slope variance of the surface; the short waves are then tilted over the distribution of these long waves. The tilting process modifies the local incidence angles as well as the polarization basis for a specific "facet" containing short waves. Although this is a somewhat heuristic approximation of emission physics, other models yield similar predictions for "long" and "short" wave effects.

In order to model WindSAT measured data, atmospheric effects must be considered in addition to direct surface emission alone; the important contributions include the upwelling atmospheric brightness, atmospheric attenuation, and reflection of the downwelling atmospheric brightness off the sea surface. Foam on the sea surface can also make significant contributions to observed brightnesses. The basic parameters of the model are then the sensor observation angles, the sensor frequency, a description of foam coverage and foam brightnesses, and a description of the atmospheric attenuation and down- and upwelling brightnesses. Additional implicit parameters of the model include the short wave sea spectrum functional form, the long wave slope probability density function, the model used for the sea water relative permittivity ϵ, and any model for long-short wave hydrodynamic modulation effects. It is typical to utilize functional forms for these quantities that reduce the relevant environmental parameters to six: the sea surface temperature (T_S), the sea water salinity (S), the wind speed (W), the azimuthal angle between the sensor look direction and the wind direction (ϕ_w), and the atmospheric columnar integrated water vapor (V) and cloud liquid water (L). Such an approach will be utilized in the results to be shown in Section IV.

Once the necessary parameters are specified, evaluation of the two-scale model requires the computation of a four-dimensional integral. Because the WindSAT dataset includes observations in a wide variety of environments, repeated computations are necessary in order to perform model and measurement comparisons. The efficiency of the two-scale model implementation then becomes critical. Although a previous work [7] has discussed an efficient two-scale model implementation, no discussion of atmospheric effects was included.

In this paper, an efficient two-scale model implementation for both direct surface emission and reflected atmospheric effects is described. The formulation is based on a tabling approach for the "weighting functions" in the formulation, eliminating repeated computations as model parameters are varied. An expansion in surface permittivity is also utilized in order to minimize the size of the required tables. Section II describes the basic formulation of the model for direct surface emission, while computation of the atmospheric reflected term is discussed in Section III. The model is then applied in Section IV in a study of sea brightnesses, and illustrates that atmospheric reflection can increase brightness azimuthal variations, rather than decrease them as is typically expected. Conclusions and a discussion of implications for the WindSAT mission are then provided in Section V.

Manuscript received Month dd, yyyy; revised Month dd, yyyy. This work was supported by the Naval Research Laboratory and the National Polar Orbiting Environmental Satellite System Integrated Program Office.

J. T. Johnson is with The Ohio State University, Dept. of Electrical and Computer Engineering and ElectroScience Laboratory.

II. Direct surface emission: Formulation

A. Large scale integration

As presented in [3], the two-scale model states that surface-only (i.e. neglecting the atmosphere) emitted brightness temperatures observed by a radiometer at polar observation angle θ can be written as

$$\overline{T}_B = \int_{-\infty}^{\infty} dS_y \int_{-\infty}^{\cot\theta} dS_x \overline{I}_{sl} \left(1 - S_x \tan\theta\right) P(S_x, S_y) \quad (1)$$

Here the vector notation indicates a 4×1 column vector containing brightnesses in the four modified Stokes' quantities: horizontal (T_h) and vertical (T_v) linear polarizations and the correlation channels U_B and V_B, respectively. Using a modification of the coordinate system of [3], the radiometer look direction is fixed along the negative x axis; variations in wind direction will later be accounted for by rotating surface properties with respect to these coordinates. The integration is over long wave slopes in the along- and cross-radiometer look directions, while the function $P(S_x, S_y)$ is the long wave slope probability density function in these coordinates. The limitation on the along-look slope to $\cot\theta$ accounts for geometric shadowing effects, and the term in the parenthesis inside the integration accounts for variations in projected facet area along the radiometer look direction. The above integration implements the long wave tilting process.

Emission from the tilted facets is described by $\overline{I}_{sl}$ in equation (1). Because received emission in a global (i.e. sensor) polarization basis is of interest, the quantity $\overline{I}_{sl}$ must be evaluated in the global basis in the slope integration. However the local facet emission is most conveniently calculated in local coordinates. A rotation matrix $\overline{\overline{R}}$ can be defined to convert the local into the global polarization basis. The needed quantity can then be written as

$$\overline{I}_{sl} = \overline{\overline{R}} \cdot \left(F_r \overline{T}_{sf} + (1 - F_r)\overline{T}_{ss}\right) \quad (2)$$

when facet emission from both foam and small scale roughness effects are included. Here F_r is the fractional area of the facet covered by sea foam, $\overline{T}_{sf}$ is the thermal emission from a completely foam covered facet, and $\overline{T}_{ss}$ is the emission from a facet with small scale roughness but no foam coverage. This approximation neglects any interaction effects between foam and surface emission; such effects have been studied using a radiative transfer model [9]. However attempting to include these contributions increases the complexity of the model and is not considered further here. It is assumed that the foam fraction F_r and foam emission $\overline{T}_{sf}$ are specified, although uncertainty in these terms remains [3], [19]. The foam coverage F_r can be allowed to be a function of the slopes S_x and S_y if an azimuthally asymmetric distribution of foam is desired, although again knowledge of such variations is incomplete at present.

The rotation matrix $\overline{\overline{R}}$ and coordinate transformation between the global and local bases are defined in Appendix A of [3]. The transformation provides knowledge of the local polar (θ_l) and azimuthal (ϕ_l) angles at which the emission from a specific facet is observed. In the current formulation, the rotation is performed in terms of radiometer look coordinate slopes (S_x, S_y). This choice allows a more efficient means of computing multiple azimuth angle observations to be developed, as will be described in the next paragraphs. The local angles (θ_l, ϕ_l) are thus defined relative to the radiometer look coordinates, and are independent of any wind direction influence. Note that although the polar angle θ_l is uniquely defined, the definition of the local azimuthal angle ϕ_l depends upon choice of the local coordinate horizontal axes. Once this choice is specified, the final rotational transformation depends only on the radiometer global observation angles (θ, ϕ) and the long wave slopes (S_x, S_y).

B. Short scale emission

Following [14], emission from the small scale roughness at local observation angles (θ_l, ϕ_l) can be written as

$$\overline{T}_{ss} = T_S \left(\begin{bmatrix} 1 - |\Gamma_h(\theta_l, \epsilon)|^2 \\ 1 - |\Gamma_v(\theta_l, \epsilon)|^2 \\ 0 \\ 0 \end{bmatrix} - \int_{k_l}^{k_u} d\tilde{k}_\rho \tilde{k}_\rho \int_0^{2\pi} d\tilde{\phi}\ \overline{g}(\tilde{k}_\rho, \tilde{\phi}, \theta_l, \epsilon)\ W(\tilde{k}_\rho, \tilde{\phi} + \phi_l) \right) \quad (3)$$

$$= T_S \left(\overline{E}_{go} + \Delta\overline{E}_{ss}\right) \quad (4)$$

in the local polarization basis. Here Γ_h and Γ_v are the horizontally and vertically polarized Fresnel reflection coefficients, W is the spectrum of the small scale roughness, and $\overline{g}$ is the second order "weighting function" from the small slope (or small perturbation method) theory, as defined in [14]. The quantities k_l and k_u represent the lower- and upper-cutoff wavenumbers of the short wave region considered. The quantity $\overline{E}_{go}$ is defined as the flat-facet emissivity, while the $\Delta\overline{E}_{ss}$ is the emissivity perturbation caused by small scale roughness.

Because the local azimuthal angle is accounted for in equation (3) by rotating the short wave spectrum, the weighting function here is evaluated at azimuth angle zero degrees. The short wave spectrum used is identical to that in the global coordinate system under this rotation; in effect the spectrum is rotated along with the facet in this process. However, the rotation transformation used in [3] attempts to minimize the change introduced in the azimuthal angle by defining the local x direction to have components in only the global $x-z$ plane. Although this choice is somewhat arbitrary, differences with other possible rotations should be small, as effects on the resulting local azimuth angles are on the order of the slope squared.

The term $\Delta\overline{E}_{ss}$ can be rewritten by introducing the curvature spectrum

$$C(\tilde{k}_\rho, \tilde{\phi}) = \tilde{k}_\rho^4 W(\tilde{k}_\rho, \tilde{\phi}) \quad (5)$$

as well as the transformation

$$\tilde{k}_\rho = 2\pi/10^l \quad (6)$$

$$l = \log_{10}\left(2\pi/\tilde{k}_\rho\right) \quad (7)$$

$$dl = -d\tilde{k}_\rho \frac{1}{\tilde{k}_\rho \ \ln 10} \quad (8)$$

$$l_b = \log_{10} \frac{2\pi}{k_u} \quad (9)$$

$$l_e = \log_{10} \frac{2\pi}{k_l} \quad (10)$$

The constant 2π values in the above equations are assumed to have the same units as $\tilde{k}_\rho$. This transformation is convenient due to the large range of length scales present in the sea surface. The modified expression is then

$$\Delta\overline{E}_{ss} = \int_{l_b}^{l_e} dl \ \frac{\ln 10}{\tilde{k}_\rho^2} \int_0^{2\pi} d\tilde{\phi} \ \overline{g}(\tilde{k}_\rho, \tilde{\phi}, \theta_l, \epsilon) \ C(\tilde{k}_\rho, \tilde{\phi} + \phi_l) \quad (11)$$

Analysis of the weighting function $\overline{g}$ shows it to have the form

$$\overline{g}(\tilde{k}_\rho, \tilde{\phi}, \theta_l, \epsilon) = \begin{bmatrix} 1 \\ 1 \\ \sin\tilde{\phi} \\ \sin\tilde{\phi} \end{bmatrix} \tilde{\overline{g}}(\tilde{k}_\rho, \cos\tilde{\phi}, \theta_l, \epsilon)^T \quad (12)$$

where the superscript T indicates the transpose operator. It is widely accepted that the short wave sea spectrum can be modeled as containing only zeroth and second cosine harmonics in azimuth:

$$C(\tilde{k}_\rho, \tilde{\phi}) = C_0(\tilde{k}_\rho) + \cos(2\left(\tilde{\phi} + \phi_w\right))C_2(\tilde{k}_\rho) \quad (13)$$

The influence of the wind direction is here included by rotating the cosine term above by ϕ_w, the relative azimuthal angle between the global radiometer look direction and the wind direction. Here $\phi_w = 0$ is defined so that the wind blows toward the radiometer. Substituting these relationships into equation (11) and simplifying yields

$$\begin{aligned}
\Delta\overline{E}_{ss} = & -2\int_{l_b}^{l_e} dl \ \frac{\ln 10}{\tilde{k}_\rho^2} \\
& \left[C_0(\tilde{k}_\rho) \int_0^{\pi} d\tilde{\phi} \begin{bmatrix} 1 \\ 1 \\ 0 \\ 0 \end{bmatrix} \tilde{\overline{g}}(\tilde{k}_\rho, \cos\tilde{\phi}, \theta_l, \epsilon)^T + \right. \\
& \cos\left(2(\phi_l + \phi_w)\right) C_2(\tilde{k}_\rho) \\
& \int_0^{\pi} d\tilde{\phi} \ \cos 2\tilde{\phi} \begin{bmatrix} 1 \\ 1 \\ 0 \\ 0 \end{bmatrix} \tilde{\overline{g}}(\tilde{k}_\rho, \cos\tilde{\phi}, \theta_l, \epsilon)^T + \\
& - \sin\left(2(\phi_l + \phi_w)\right) C_2(\tilde{k}_\rho) \\
& \left. \int_0^{\pi} d\tilde{\phi} \ \sin 2\tilde{\phi} \begin{bmatrix} 0 \\ 0 \\ \sin\tilde{\phi} \\ \sin\tilde{\phi} \end{bmatrix} \tilde{\overline{g}}(\tilde{k}_\rho, \cos\tilde{\phi}, \theta_l, \epsilon)^T \right] \quad (14) \\
= & \int_{l_b}^{l_e} dl \ C_0(\tilde{k}_\rho)\overline{M}_0(\tilde{k}_\rho, \theta_l, \epsilon) + \\
& \cos\left(2(\phi_l + \phi_w)\right) \begin{bmatrix} 1 \\ 1 \\ 0 \\ 0 \end{bmatrix} \\
& \int_{l_b}^{l_e} dl \ C_2(\tilde{k}_\rho)\overline{M}_{2c}(\tilde{k}_\rho, \theta_l, \epsilon)^T + \\
& \sin\left(2(\phi_l + \phi_w)\right) \begin{bmatrix} 0 \\ 0 \\ 1 \\ 1 \end{bmatrix} \\
& \int_{l_b}^{l_e} dl \ C_2(\tilde{k}_\rho)\overline{M}_{2s}(\tilde{k}_\rho, \theta_l, \epsilon)^T \quad (15)
\end{aligned}$$

The $\overline{M}$ quantities involve the integrations over $\tilde{\phi}$ in equation (14), and depend only on the dummy wavenumber $\tilde{k}_\rho$, the local polar observation angle θ_l, and the surface permittivity ϵ. It is therefore possible to create a table of these quantities for a set of parameters to avoid repeated computations as the surface spectrum (i.e. windspeed) is varied. A tabling code was developed to perform this process, and stored the $\overline{M}$ functions for θ_l values from 0 to 88 degrees in 2 degree steps. Results from the table were linearly interpolated in θ_l to obtain predictions for general local polar angles. The tabling code also utilized 1000 points in l between l_b and l_e values corresponding to $k_l = k_0/10$ and $k_u = 10k_0$, where k_0 is the electromagnetic wavenumber. The integration over $\tilde{\phi}$ was performed using a simple pulse-rule with 1024 points; this large number of points was chosen to ensure that any "critical phenomenon" type behaviors [14] were resolved in the calculations. Tests performed showed these choices to provide accurate computations for the cases considered here, although a smaller number of points in both l and $\tilde{\phi}$ would likely retain sufficient accuracy as well.

It is also desireable to remove the permittivity dependence from the tabled values, so that the table computations need not be repeated when the sea surface temperature or salinity are modified. This was performed by expanding the $\tilde{\overline{g}}$ weighting functions in a second-order, two-dimensional Taylor series in the real and imaginary parts of the relative permittivity. Derivatives in this expansion were also integrated over azimuth and stored in the table. The expansion point in the process was chosen to correspond to the sea water permittivity at a particular (T_S, S) value. The choice $T_S = 290$ K, $S = 34$ psu was found to yield high accuracy for a wide range of T_S values when using the second order expansion. It is also possible to incorporate Taylor series expansions about two separate (T_S, S) bias points in the table, so that accuracy can be enhanced for a wider range of T_S values.

C. Final algorithm

The final code then consists of a "table-making" routine that generates tables of the $\tilde{\phi}$ integrated, Taylor expanded quantities, and a "calculation" code that reads in the tables and computes two-scale predictions of brightness temperatures. The calculation code implements the

$$\overline{T}_B = T_S \int_{-\infty}^{\infty} dS_y \int_{-\infty}^{\cot\theta} dS_x \left(1 - S_x \tan\theta\right) P(S_x, S_y, \phi_w)\overline{\overline{R}} \cdot \left(\overline{E}_{go} + \Delta\overline{E}_{ss}\right) \quad (16)$$

equation; foam effects are ignored above for simplicity. This can be separated into a geometrical-optics term

$$\overline{T}_{B,go} = T_S \int_{-\infty}^{\infty} dS_y \int_{-\infty}^{\cot\theta} dS_x \,(1 - S_x \tan\theta) \; P(S_x, S_y, \phi_w) \overline{\overline{R}} \cdot \overline{E}_{go} \quad (17)$$

and a tilted-small scale roughness term

$$\Delta\overline{T}_{B,ss} = T_S \int_{-\infty}^{\infty} dS_y \int_{-\infty}^{\cot\theta} dS_x \,(1 - S_x \tan\theta) \; P(S_x, S_y, \phi_w) h(S_x, \phi_w) \overline{\overline{R}} \cdot \Delta\overline{E}_{ss} \quad (18)$$

The geometrical optics term is not expensive to evaluate, and so is computed without additional approximation for the exact permittivity desired. The tilted small scale term remains more expensive even with the tabling procedure due to the integration over l. However note that relative wind direction effects are outside the integration in equation (15); this enables more efficient computations when multiple wind directions are considered simultaneously in the large scale roughness integration.

Because the large scale slope probability density function (pdf) is typically modeled as Gaussian or near-Gaussian, it is convenient to utilize a Gauss-Hermite quadrature in performing the large scale slope integration. Wind direction effects are accounted for by rotating the slope pdf from the along- and cross- wind coordinates to the along- and cross- look coordinates. This results in a wind direction dependent term within the large scale integration but outside the integration over l. The hydrodynamic modulation term $h(S_x, \phi_w)$ of [3] has also been introduced in equation (18), but is also outside the integration over l. In the results to be illustrated in Section IV, relative wind direction angles of $0, 15, ..., 180$ degrees were utilized simultaneously in the slope integration, along with 32 by 32 points in the Gauss-Hermite quadrature.

Using this approach, the table making code needs to be run only once for a given radiometer frequency. The calculation code can then compute two-scale model predictions for other parameter choices, including wind speed and direction, short wave spectral model, long wave slope PDF model, hydrodynamic modulation model, sea surface temperature, sea salinity, or radiometer observation angle.

III. Reflected Atmospheric Brightness: Formulation

A. General equations

The reflection of downwelling atmospheric emission is another contribution to the WindSAT observed brightnesses that must be modeled in order to capture wind direction effects accurately [5],[20]. Neglecting foam effects, the reflected downwelling atmospheric emission can be written as

$$\overline{T}_R = \overline{T}_{R,go} + \Delta\overline{T}_{R,ss} \quad (19)$$

with

$$\overline{T}_{R,go} = \int_{-\infty}^{\infty} dS_y \int_{-\infty}^{\cot\theta} dS_x \,(1 - S_x \tan\theta) \; P(S_x, S_y, \phi_w) T_{DN}(\theta') \overline{\overline{R}} \cdot \overline{R}_{go} \quad (20)$$

and

$$\Delta\overline{T}_{R,ss} = \int_{-\infty}^{\infty} dS_y \int_{-\infty}^{\cot\theta} dS_x \,(1 - S_x \tan\theta) \; P(S_x, S_y, \phi_w) h(S_x, \phi_w) \overline{\overline{R}} \cdot \Delta\overline{R}_{ss} \quad (21)$$

Here $\overline{R}_{go}$ includes the Fresnel reflection terms only in equation (3), and $T_{DN}(\theta')$ is the downwelling atmospheric brightness at angle θ', defined by

$$k_0 \cos\theta' = -\hat{z} \cdot \left(\overline{k} - 2\hat{n}\left(\hat{n} \cdot \overline{k}\right)\right) \quad (22)$$

with the radiometer location vector $\overline{k}$ and surface normal $\hat{n}$ as defined in [3]. The geometrical optics term remains inexpensive to compute.

The tilted small scale roughness term now involves

$$\Delta\overline{R}_{ss} = \int_{k_l}^{k_u} d\tilde{k}_\rho \tilde{k}_\rho \int_0^{2\pi} d\tilde{\phi} \; W(\tilde{k}_\rho, \tilde{\phi} + \phi_l) \Big\{ \overline{g}_{rc}(\tilde{k}_\rho, \tilde{\phi}, \theta_l, \epsilon) \; T_{DN}(\theta') + \overline{g}_{ri}(\tilde{k}_\rho, \tilde{\phi}, \theta_l, \epsilon) \; T_{DN}(\tilde{\theta}) \Big\} \quad (23)$$

Here the coherent g_{rc} and incoherent g_{ic} terms are separated in the weighting functions of [14], because the coherent term applies to the sky brightness at the specular angle θ', while the incoherent term couples sky brightnesses at angle $\tilde{\theta}$, defined by

$$k'_x = k_{xl} + \tilde{k}_\rho \cos\tilde{\phi} \quad (24)$$

$$k'_y = k_{yl} + \tilde{k}_\rho \sin\tilde{\phi} \quad (25)$$

$$k_{z'} = -\sqrt{k_0^2 - k_x'^2 - k_y'^2} \quad (26)$$

$$\overline{K} = \overline{\overline{R}}^{-1} \cdot \overline{k}' \quad (27)$$

$$K_\rho = \sqrt{K_x^2 + K_y^2} \quad (28)$$

$$k_0 \sin\tilde{\theta} = K_\rho \quad (29)$$

The above equations involve $\overline{k}_l$, the radiometer location vector in the local coordinates, $\overline{k}'$, the propagation direction of the downwelling atmospheric brightness in the local coordinates, and $\overline{K}$, the projection of this vector into the global coordinate system.

Unlike the case of surface-only emission, where all needed quantities were tilted along with the surface facet, the atmospheric brightness is not tilted with the facet, but remains specified in the global coordinate system. This results in a slope term inside the short wave spectrum integrations that is not easily decoupled. An alternative approach is required in order to develop an efficient algorithm.

B. Tabling in slope

An efficient algorithm can be developed if a fixed radiometer polar observation angle θ is assumed. In this case, a table of azimuthally integrated weighting functions can be generated for a set of long wave slopes S_x and S_y as opposed to a set of local polar incidence angles. For specified long wave slopes, the rotational transformation is fixed, and the computation of $\tilde{\theta}$ is known in terms of $\tilde{\phi}$. If the atmospheric downwelling

brightness is specified, a table can be constructed to eliminate repeated computations as surface parameters are varied.

The form of the integration for the coherent and incoherent terms remains similar to that in equation (14), but the incoherent term includes the azimuthally varying sky brightness. For this reason, some of the azimuthal symmetries in the direct surface emission case are not applicable. First, because ϕ_l is constant when considering fixed slopes, the ϕ_l rotation on the weighting function in equation (14) is not performed, i.e. the weighting functions are evaluated at azimuthal angle ϕ_l instead of 0 degrees, and the spectrum is not rotated by ϕ_l. The azimuthal integrations remain from 0 to 2π, and the terms inside the brackets in equation (14) are replaced by

$$\begin{bmatrix} 1 \\ 1 \\ \sin(\tilde{\phi} - \phi_l) \\ \sin(\tilde{\phi} - \phi_l) \end{bmatrix} \tag{30}$$

for both integrations, now multiplying cosine and sine variations in ϕ_w. Although this apparently results in the possibility of sine harmonics in the linearly polarized channels as well as cosine harmonics in the correlation channels, the final terms remain zero due to cancellation as the local azimuth angle is varied. Note variations with wind direction still remain outside the integrations over length scale, so that multiple wind directions can be considered efficiently.

After these modifications, tabulated functions similar to the $\overline{M}$ functions in equation (15) can be defined; it is advantageous to tabulate the the coherent and incoherent terms separately due to their separate dependencies on the sky brightness. A Taylor series expansion in permittivity is again utilized, although truncation of the expansion to first order only was found sufficiently accurate for reflected brightness computations.

The table in slopes was generated using 11 by 11 points from $S = -0.8$ to $S = 0.8$; these limits represent (one-dimensional) tilt angles up to 38.6 degrees so that a wide range of tilt variations is included. Weighting functions were set to zero for tilt angles outside this range. An odd number of points in the table was chosen to ensure that the untilted case was included as a point in the tabling process. Tests comparing results with those not utilizing the table showed agreement to within less than 0.1 K over a realistic range of windspeeds. Interpolation in the table is performed using a second order interpolation in two dimensions based on 9 points in the table surrounding the point of interest. The final interpolation is performed first in permittivity, then in slope.

C. Modeling the downwelling atmospheric brightness

The above description enables an efficient code to be developed, again in terms of a "tabling" code and a "calculating" code, but in this case it is required that the radiometer polar observation angle be fixed when generating the tables. It is also required that the downwelling atmospheric brightness be known when computing the integrations over $\tilde{\phi}$. Although the downwelling brightness in general is a complicated function of polar angle, it is common practice to model the atmosphere in terms of an equivalent one-layer, planar medium. The resulting downwelling brightness is then

$$T_{DN}(\theta) = T_{air}\left(1 - e^{-\alpha \sec\theta}\right) \tag{31}$$

where T_{air} is the effective physical temperature of the one layer medium and α is the effective zenith attenuation in Nepers. The two parameter nature of this function is attractive, as well as the fact that one of the parameters (T_{air}) is a simple multiplicative term that is easily factored out.

When computing the reflection of downwelling brightness in the two-scale model, modeling the downwelling variations with polar angle accurately is important because all downwelling angles are scattered into the radiometer observation direction. It is well known that the one-layer model is generally applicable for polar angles less than approximately 80 degrees, while at larger polar angles, spherical Earth effects must be included and the simple form of equation (31) is not retained. To investigate these issues, a test of reflected atmospheric brightnesses was performed using planar and spherical Earth downwelling brightness models. Spherical Earth predictions were computed using a spherical-Earth radiative transfer code [21] for a fairly attenuative atmosphere resulting in a downwelling brightness at 55 degrees of approximately 150 K. Equation (31) was fit to the numerically computed spherical Earth brightness, using polar angles 0 to 80 degrees in the fitting process. The results were in agreement to within 0.34 K for this range of angles using an effective air temperature of 274 K and zenith attenuation 0.46 Nepers, but differences up to 17.5 K were obtained at larger angles. However, two-scale model computations of reflected brightnesses for a range of wind speeds were in agreement to within 0.1 K. These results, though from a single test only, suggest that the planar one layer model may be sufficient for most applications.

Because the one-layer model has only a single parameter, it is possible to include variations with α in the tabling process so that multiple atmospheric downwelling profiles can be considered without repeated tabling computations. This is performed simply by computing multiple tables in slope for a set of α values. Because the relative amplitude of α can vary significantly with atmospheric conditions, the set of alpha values was generated linearly in $\log_{10}\alpha$, with values ranging from -2.4 ($\alpha = 0.004$) to -0.2 ($\alpha = 0.631$). A second-order interpolation was performed in α using three table points surrounding the point of interest; this interpolation was performed prior to both the permittivity and slope interpolations discussed previously.

D. Slope integration

The final calculation code now performs the integrations over (S_x, S_y) and l, as in the direct surface emission case. However, the slope integration in this case is complicated by abrupt discontinuities as the specular angle θ' crosses 90 degrees, beyond which the atmospheric brightness is zero. These discontinuities make Gauss-Hermite quadrature inappropriate, and instead a Gauss-Legendre quadrature was adopted. Even with this modification, treatment of the transition region around $\theta' \approx 90$ degrees still requires special care.

To address this problem, the slope integration was first transformed to polar coordinates (S_ρ, ϕ_s). It can be shown that $\theta' \approx 90$ degrees does not occur for $S_\rho < \sec\theta - \tan\theta = S_1$; a Gauss-Legendre quadrature using 9 points was then utilized from $S_\rho = 0$ to this boundary, along with a simple pulse integration in azimuth using 16 points. A second Gauss-Legendre quadrature was utilized for $S_\rho = S_1$ to 4 times the rms slopes of the slope PDF; in this region a modified azimuthal pulse integration was used in which portions of the integration within approximately 45 degrees of the transition point $\theta' = 90$ degrees were sampled at a 4 times finer rate than that of the previous azimuthal integration. Results showed this method to provide reasonable accuracy at resolving the transition region in the reflected downwelling brightness computation.

IV. Results

Although results from two-scale model computations of direct surface emission have been reported previously [1]-[10], the reflected downwelling atmospheric brightness has been examined in a smaller number of studies [5],[20]. The current formulation allows this term to be computed efficiently for a wide variety of surface and atmospheric conditions.

The results presented in this section were computed using the Durden-Vesecky model of the sea spectrum [22], but with an amplitude of $a_0 = 0.0049$ as opposed to the $a_0 = 0.008$ typically used in previous emission studies. In addition, the hydrodynamic modulation term $h(S_x, \phi_w)$ was defined in terms of the upwind slopes as in [3] but modified to take on minimum and maximum values of 0 and 2, respectively, as opposed to the 0.5 to 1.5 range of [3]. The cutoff wavenumber was chosen as $k_0/2.2$, and a Gaussian model of the long wave slope pdf was utilized. Foam effects were neglected, as well as the influence of the downwelling cosmic background brightness, although both of these effects can be easily included after computations are completed if the foam fraction is assumed independent of slope; see [23] for means for including the cosmic background term. The "modified Stogryn" model of the sea permittivity is used [24], with a fixed sea water salinity of 34 psu. Choice of these parameters is described in [11]. Up- and downwelling atmospheric brightnesses and atmospheric attenuation were parametrized in terms of the V, L, and T_S quantities following the approach described in [23], along with an assumed cloud temperature of 280 K. The WindSAT 18.7 GHz channel is studied, with computations performed at the nominal incidence angle of 55.8 degrees.

Figure 1 plots azimuthal variations in all four polarimetric channels for windspeed $W = U_5 = 10$ m/s, $T_S = 300$ K, and downwelling atmospheric parameters ($T_{air} = 286.6$ K, $\alpha = 0.076$). These correspond to an integrated water vapor content of $V = 48$ mm and $L = 0$ mm. Results at surface level are plotted for both the surface only case and the case including the reflected downwelling brightness. Here average values of 82.3 K and 176.2 K are removed from the horizontal and vertical surface only cases, with corresponding average values of 114.1 and 192.2 K removed when the atmosphere is included. Results show the azimuthal variations to be slightly impacted by the presence of this moderately attenuating atmosphere, particularly in the U brightness.

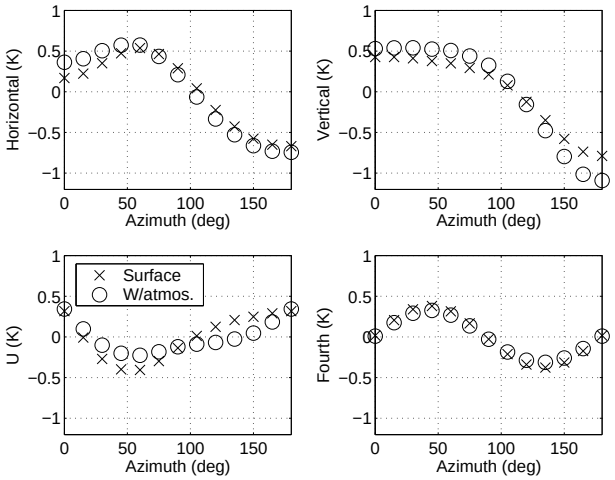

Fig. 1. Azimuthal variations of total brightnesses at surface level: 18.7 GHz, $T_S = 300$ K, $V = 48$ mm, $L = 0$ mm, Wind speed 10 m/sec

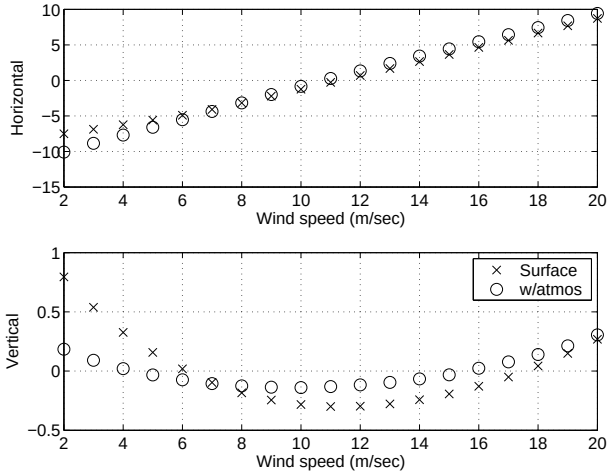

Fig. 2. Zeroth azimuthal harmonics of surface level brightnesses, versus wind speed: 18.7 GHz, $T_S = 300$ K, $V = 48$ mm, $L = 0$ mm.

The total atmospheric brightnesses obtained are still well fit by the standard cosine (for linear channels) and sine (for correlation channels) expansions in the relative azimuth angle. Figures 2 through 4 illustrate the obtained azimuthal zeroth, first, and second harmonics with and without the reflected atmosphere, again at surface level. Mean values of the curves (83.5 K horizontal, 176.5 K vertical, no atmosphere, 114.9 K horizontal, 192.3 K vertical, with atmosphere) are again removed from the zeroth harmonics so that the dependence on wind speed can be seen more easily. The atmosphere is seen to influence the windspeed dependence of all harmonics, and to have the capability of enhancing surface-only azimuthal harmonic coefficient amplitudes.

A. An approximation for the reflected brightness

A simple approximation that is used to model the reflected downwelling term assumes that the atmospheric brightness can be modeled as a constant

$$T_{DN}(\theta') = T_{DN}(\theta) \tag{32}$$

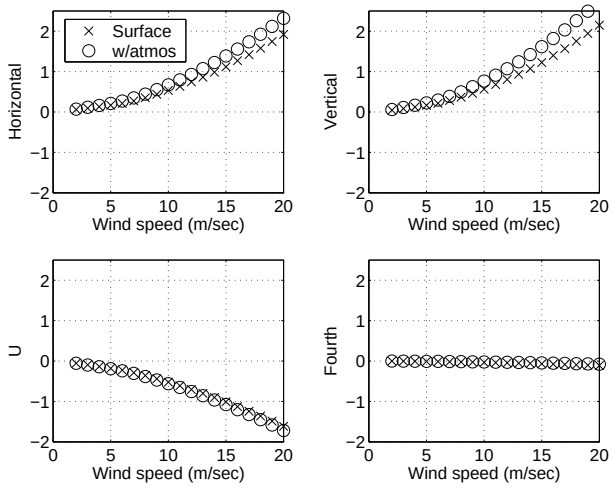

Fig. 3. Same as Figure 2, but for first azimuthal harmonics

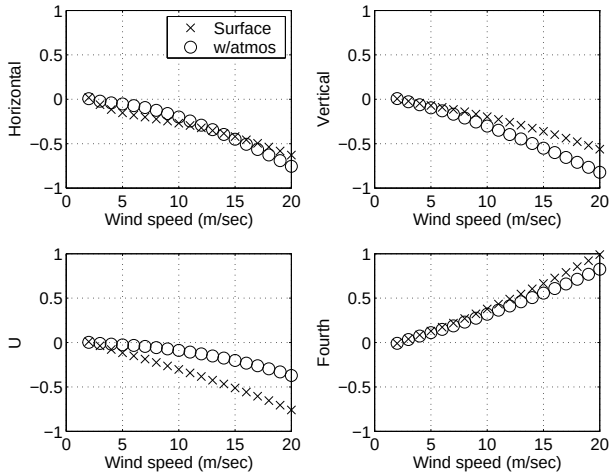

Fig. 4. Same as Figure 2, but for second azimuthal harmonics

where θ is the radiometer polar observation angle. In this case, the reflected brightness computation becomes almost identical to the direct surface emission computation, since T_{DN} no longer varies with angle. The approximate reflected brightness simplifies to

$$\overline{T}_{R,a} = T_{DN}(\theta) \left(\begin{bmatrix} 1 \\ 1 \\ 0 \\ 0 \end{bmatrix} - \overline{T}_B / T_S \right) \tag{33}$$

It is apparent that under this approximation the reflected atmosphere term can only reduce amplitudes of the surface-only azimuthal harmonic variations, due to the opposing relationship with $\overline{T}_B$. A multiplicative correction to this approximation involving a term defined as $\overline{\Omega}$ is proposed in [23]. An empirical process was used to determine the form of $\overline{\Omega}$ in [23] for horizontal and vertical polarizations only; the form determined did not involve any variations with azimuth. Here a similar form is utilized, but for all polarimetric brightnesses and including azimuthal variations.

To simplify azimuthal variation effects, $\overline{\Omega}$ is now defined in terms of the azimuthal harmonic coefficients of the approximate reflected and direct surface emitted brightnesses, through

$$\overline{T}_{R,i} \approx \overline{T}_{R,a,i} \left(1 + \overline{\Omega}_i^T \right) \tag{34}$$

where the subscript $i = 0, 1,$ or 2 indicates the azimuthal harmonic coefficient of the term considered. The above equation provides a definition of the ith azimuthal harmonic coefficient of $\overline{\Omega}$. Due to the cancellation of the effective air temperature of the downwelling brightness, T_{air}, only α is required to describe the atmospheric state in computing $\overline{\Omega}$. However, $\overline{\Omega}$ remains a function of all remaining model parameters, including the sea surface spectrum model utilized.

Figure 5 illustrates plots of $\overline{\Omega}_0$ versus windspeed for $T_S = 295$ K and for $\alpha = 0.022$ and $\alpha = 0.148$. The smooth curves obtained versus windspeed are qualitatively similar to the empirical forms in [23]. Note that horizontal polarization has a larger correction than vertical, due to the stronger reflection of atmospheric brightness in this polarization, and that the magnitude of $\overline{\Omega}_0$ decreases as the atmosphere becomes more dense.

Figure 6 plots $\overline{\Omega}_1$ values versus windspeed in all polarimetric channels. Here large negative values are observed in

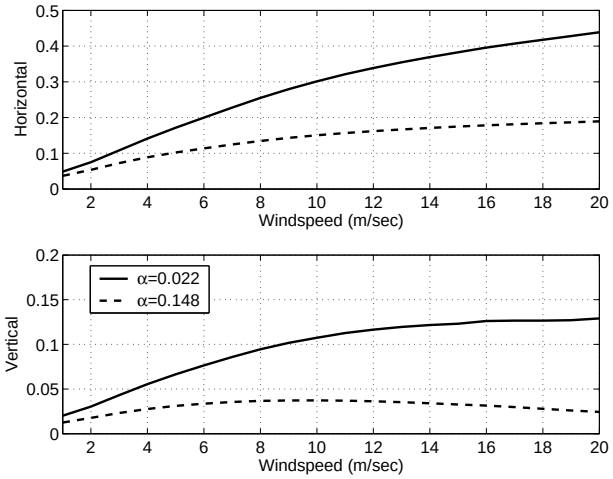

Fig. 5. $\overline{\Omega}_0$ versus wind speed: 18.7 GHz, $T_S = 295$ K

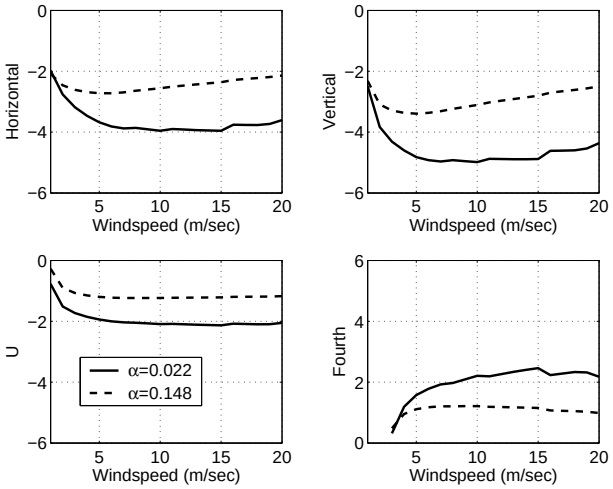

Fig. 6. $\overline{\Omega}_1$ versus wind speed: 18.7 GHz, $T_S = 295$ K

all cases except the fourth Stokes parameter. These negative values indicate that the reflected downwelling brightness is increasing, rather than decreasing, total azimuthal first harmonic variations. Again the amplitudes of $\overline{\Omega}$ are observed to decrease for the denser atmosphere. The non-smooth behavior observed in the curves at higher windspeeds is likely due to computational errors; the size of these errors is not significant when utilizing $\overline{\Omega}$ in a final brightness computation.

Second azimuthal harmonics of $\overline{\Omega}$ are illustrated in Figure 7. Both large positive and negative values are observed, indicating the reflected atmospheric brightness can either decrease or increase total second harmonic variations depending on the polarization considered. Note the second harmonic of vertical polarization is of particular interest due to the typically small values obtained in this channel from direct surface emission only near the nominal polar observation angle of 55.8 degrees.

V. Conclusions

The model proposed in this paper can be utilized in studies of sea surface emission for numerous future radiometer missions. The approach described provides efficient computations

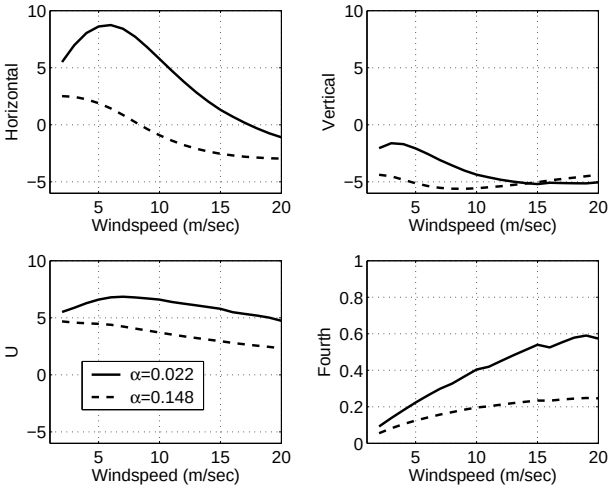

Fig. 7. $\overline{\Omega}_2$ versus wind speed: 18.7 GHz, $T_S = 295$ K

by tabling repeated calculations, and by utilizing Taylor series expansions when appropriate. A study utilizing this algorithm in a comparison with WindSAT data is currently in progress. Further studies of the number of points and interpolation schemes utilized could likely improve computational efficiency beyond that of the current implementation.

A study of reflected downwelling brightness performed with this code showed that this term can make appreciable contributions to measured brightnesses. It was also shown that the reflected downwelling brightness can either decrease or increase measured azimuthal variations depending on the properties of the sea and atmosphere. Because it is highly desirable to remove atmospheric influence when performing sea wind vector retrievals, these results show that careful consideration will be required in order to develop an effective atmospheric cancellation method. The results for $\overline{\Omega}$ provided could be used to develop such a method, however the results shown were computed only for a specific model of the sea surface that has yet to be validated versus measured data. Efforts to improve the code will continue in order to provide a validated description of the $\overline{\Omega}$ term.

Acknowledgment

The author would like to thank the Naval Research Laboratory WindSAT team (Drs. Mike Bettenhausen, Nai-Yu Wang, Magdalena Anguelova, and Peter Gaiser) for assistance in model evaluation studies. Mr. Metin Demir of The Ohio State University is also thanked for assistance with performing the computations.

References

[1] Gaiser, P. W. et al, "The WindSAT spaceborne polarimetric microwave radiometer: sensor description and early orbit performance," *IEEE Trans. Geosc. Remote Sens.*, vol. 42, pp. 2347-2361, 2004.

[2] Yueh, S. H., S. V. Nghiem, and R. Kwok, "Comparison of a polarimetric scattering and emission model with ocean backscatter and brightness measurements," *IGARSS'94*, conference proceedings, 1994.

[3] Yueh, S. H., "Modeling of wind direction signals in polarimetric sea surface brightness temperatures," '*IEEE Trans. Geosc. Remote Sens.*, vol. 35, pp. 1400-1418, 1997.

[4] P. Coppo, J. T. Johnson, L. Guerriero, J. A. Kong, G. Macelloni, F. Marzano, P. Pampaloni, N. Pierdicca, D. Solimini, C. Susini, G. Tofani, and Y. Zhang, "Polarimetry for Passive Remote Sensing," Final Report for European Space Agency Contract 11446/956/NL/NB, Centro di Telerilevamento a Microonde, Firenze, Italy, December 1996.
[5] Pierdicca, N., F. S. Marzano, L. Guerriero, and P. Pampaloni, "On the effect of atmospheric emission upon the passive microwave polarimetric response of an azimuthally anisotropic sea surface," *Progress in Electromagnetics Research (PIER) 26*, Ed. J. A. Kong, pp. 223-248, 2000.
[6] Dinnati, E. P., J. Boutin, G. Caudal, J. Etcheto, and P. Waldteufel, "Influence of sea surface emissivity model parameters at L-band for the estimation of salinity," *Int. J. Rem. Sens.*, vol. 23, pp. 5117-5122, 2002.
[7] Lyzenga, D. R. and J. F. Vesecky, "Two-scale polarimetric emissivity model: efficiency improvements and comparisons with data," *Progress in Electromagnetics Research (PIER) 37*, pp. 205–219, J. A. Kong, ed., Cambridge: EMW Publishing, 2002.
[8] St. Germain, K., G. A. Poe, and P. W. Gaiser, "Polarimetric emission model of the sea at microwave frequencies and comparison with measurements," *Progress in Electromagnetics Research (PIER) 37*, pp. 1–30, J. A. Kong, ed., Cambridge: EMW Publishing, 2002.
[9] Zhang, Y., Y. E. Yang, and J. A. Kong, "A composite model for estimation of polarimetric thermal emission from foam-covered wind-driven ocean surface," *Progress in Electromagnetics Research (PIER) 37*, pp. 143–190, J. A. Kong, ed., Cambridge: EMW Publishing, 2002.
[10] J. T. Johnson, W. H. Theunissen, and S. W. Ellingson, "A study of sea emission models for WindSAT," *IGARSS'03*, conference proceedings, 2003.
[11] Bettenhausen, M. H., C. K. Smith, R. M. Bevilacqua, N. Wang, P. W. Gaiser, and S. Cox, "A nonlinear optimization algorithm for WindSAT wind vector retrievals," submitted to *IEEE Trans. Geosc. Rem. Sens.*, 2005.
[12] Kunkee, D. B. and A. J. Gasiewski, "Simulation of passive microwave wind direction signatures over the ocean using an asymmetric-wave geometrical optics model," *Radio Science*, Vol. 32, pp. 59, 1997.
[13] Irisov, V. G., "Small-slope expansion for thermal and reflected radiation from a rough surface," *Waves in Random Media*, vol. 7., pp. 1-10, 1997.
[14] Johnson, J. T., and M. Zhang, "Theoretical study of the small slope approximation for ocean polarimetric thermal emission," *IEEE Trans. Geosc. Remote Sens.*, vol. 37, pp. 2305–2316, 1999.
[15] Johnson, J. T. and Y. Cai, "A theoretical study of sea surface up/down wind brightness temperature differences," *IEEE Trans. Geosc. Remote Sens.*, vol. 40, pp. 66–78, 2002.
[16] Johnson, J. T., "A study of ocean-like surface thermal emission and reflection using Voronovich's small slope approximation," accepted by *IEEE Trans. Geosc. Remote Sens.*, 2005.
[17] J. T. Johnson, R. T. Shin, J. A. Kong, L. Tsang, and K. Pak, "A numerical study of ocean polarimetric thermal emission," *IEEE Trans. Geosc. Remote Sens.*, vol. 37, no. 1 (part I), pp. 8–20, 1999.
[18] Li, S. Q., C. H. Chan, M. Y. Xia, B. Zhang, and L. Tsang, "Multilevel expansion of the sparse-matrix canonical grid method for two-dimensional random rough surfaces," *IEEE Trans. Ant. Prop.*, vol. 49, pp. 1579–1589, 2001.
[19] Rose, L. A. et al, "Radiometric measurements of the microwave emissivity of foam," *IEEE Trans. Geosc. Rem. Sens.*, vol. 40, pp. 2619–2625, 2002.
[20] Yeang, C. P., S. H. Yueh, K. H. Ding, and J. A. Kong, "Atmospheric effect on microwave polarimetric passive remote sensing of ocean surfaces," *Radio Science*, vol. 34 (2), pp. 521–537, 1999.
[21] Wang, N., personal communication, 2004.
[22] Durden, S. L. and J. F. Vesecky, "A physical radar cross-section model for a wind driven sea with swell," *IEEE J. Oceanic Eng.*, vol. OE-10, pp. 445–451, 1985.
[23] Wentz, F. J. and T. Meissner, "Algorithm theoretical basis document: AMSR Ocean algorithm, version 2," report from Remote Sensing Systems, Inc., available at *www.remss.com*.
[24] Stogryn, A., "Equations for the permitivity of sea water," Naval Research Laboratory report, code 7223, Aug 1997.

Joel T. Johnson (S'88-M'96-SM'03) received the bachelor of electrical engineering degree from the Georgia Institute of Technology in 1991 and the S.M. and Ph.D. degrees from the Massachusetts Institute of Technology in 1993 and 1996, respectively. He is currently an associate professor in the Department of Electrical and Computer Engineering and ElectroScience Laboratory of The Ohio State University. His research interests are in the areas of microwave remote sensing, propagation, and electromagnetic wave theory. Dr. Johnson is a member of commissions B and F of the International Union of Radio Science (URSI), and a member of Tau Beta Pi, Eta Kappa Nu, and Phi Kappa Phi. He received the 1993 best paper award from the IEEE Geoscience and Remote Sensing Society, was named an Office of Naval Research Young Investigator, National Science Foundation Career awardee, and PECASE award recipient in 1997, and was recognized by the U. S. National Committee of URSI as a Booker Fellow in 2002.